Autocorrelation Analysis of the Seismic Data Recorded on Mars

Sizhuang Deng* and Alan Levander

Department of Earth, Environmental and Planetary Sciences, Rice University, Houston, TX, USA; * Email: sd62@rice.edu

Introduction

In this study we applied the autocorrelation method on the continuous ambient noise seismic data recorded by InSight seismic station (SEIS) to retrieve two types of seismic phases on Mars, body-wave reflection signals and planet orbiting surface wave. The depths of several seismic boundaries, including crust-mantle boundary (Moho), olivine-wadsleyite transition and core-mantle boundary (CMB), are estimated from the depth conversion of body-wave reflection responses (Deng and Levander, 2020). The planet orbiting surface wave can be used to constrain the upper mantle velocity model of Mars (Deng and Levander, 2022). The results in our study are consistent with the observations from other studies.

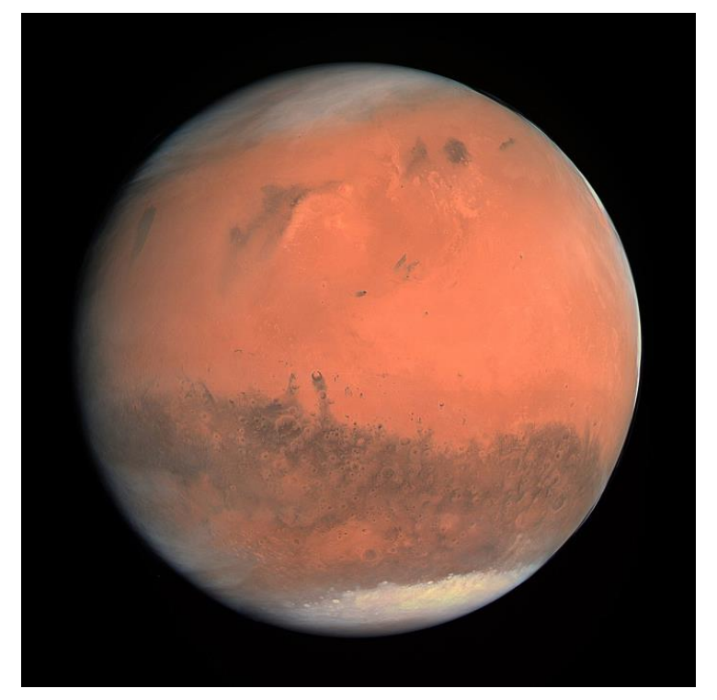

https://en.wikipedia.org/wiki/Mars

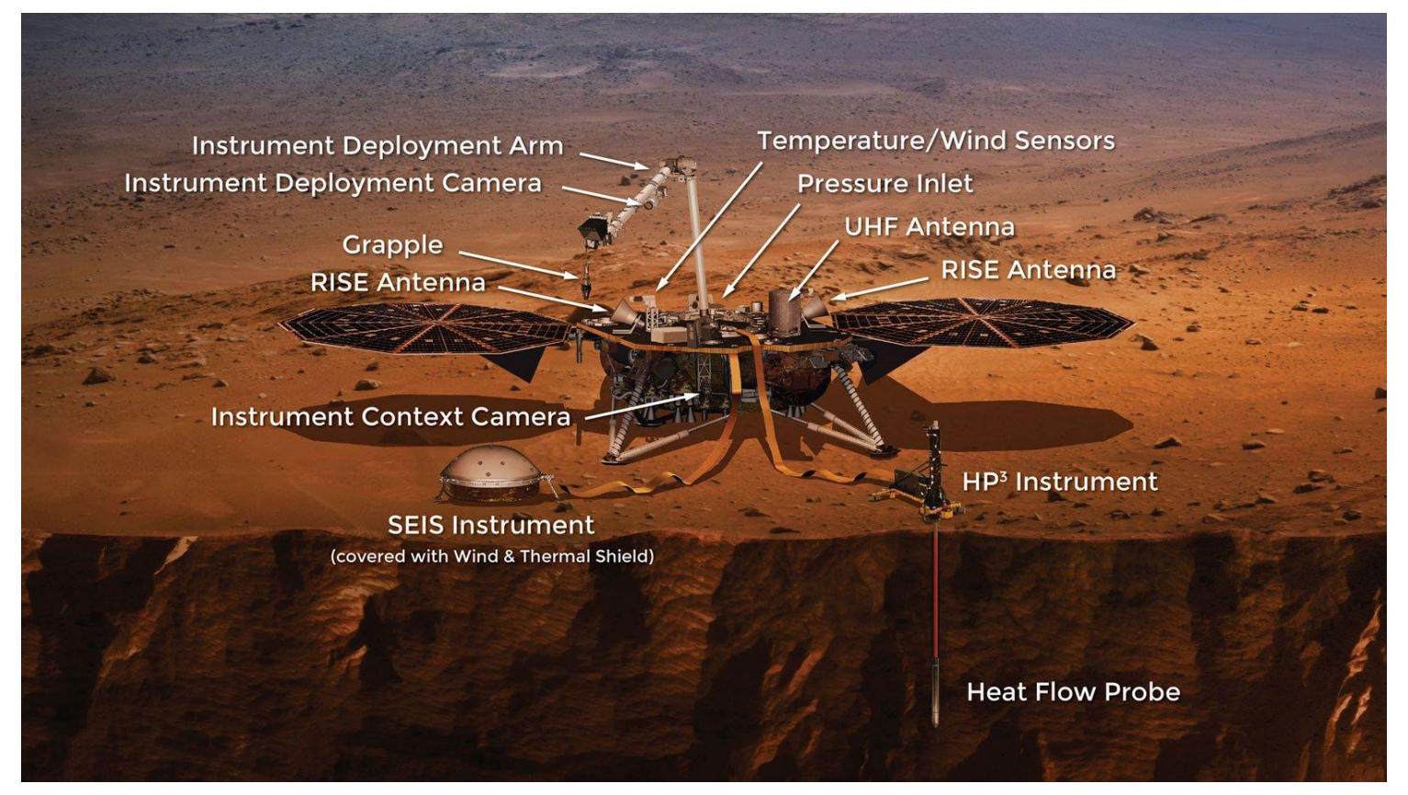

https://mars.nasa.gov/insight/spacecraft/instruments/summary/

Autocorrelation Theory

1. The Reflection Signal from Surface Source is Equivalent to the Autocorrelation of the Transmission Signal from a Deep Plane-Wave Source (Claerbout, 1968)

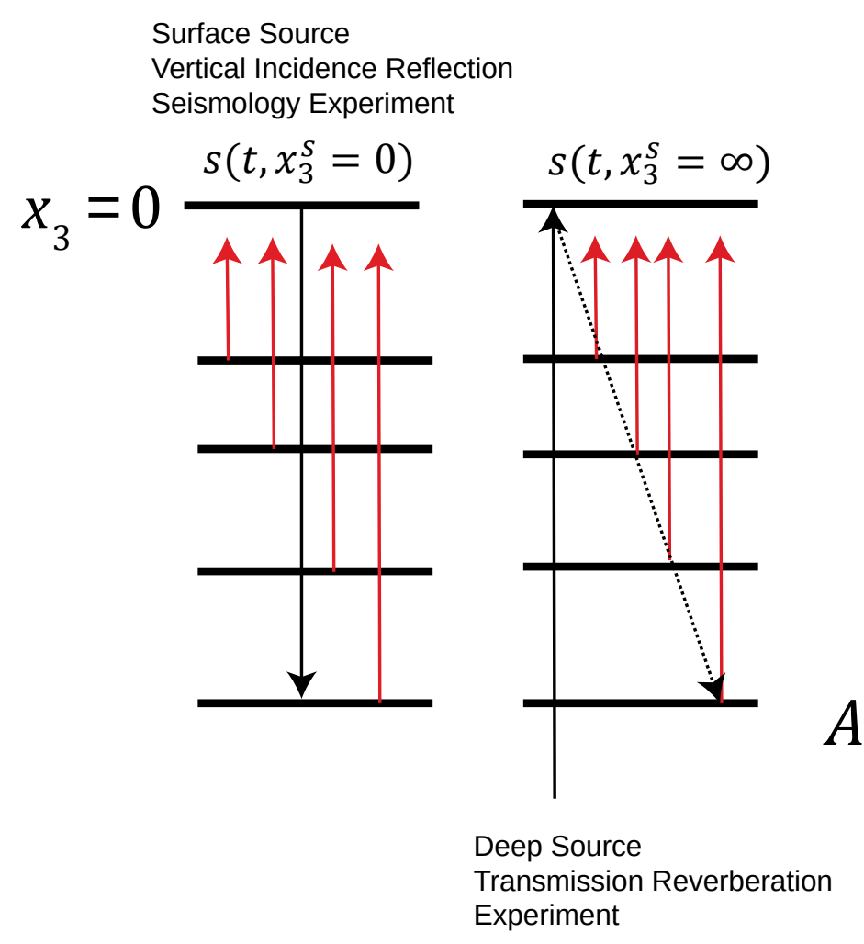

$$S(t,x_3^s=0)=R(t,x_3^s=0)*w(t)$$

Deconvolution — Active Source on Surface

$$R(t,x_3^s=0)=s(t,x_3^s=0)*w^{-1}(t)$$

$$A(Z,x_3^s=\infty)=\left(1+R(Z)+R\left(\frac{1}{Z}\right)\right)W(Z)$$

Inverse Z-Transform — Passive Source from Bottom

$$A(t,x_3^s=\infty)=\big(\delta(t)+R(t)+R(-t)\big)*W(t)$$

$s(t,x_3^s=\yen)$ Can be a signal from a teleseismic earthquake or it can be *background noise*

2. Ambient Noise Autocorrelation from single station can retrieve the surface waves (R_2) that travel around the planet for one cycle (Schimmel et al., 2018)

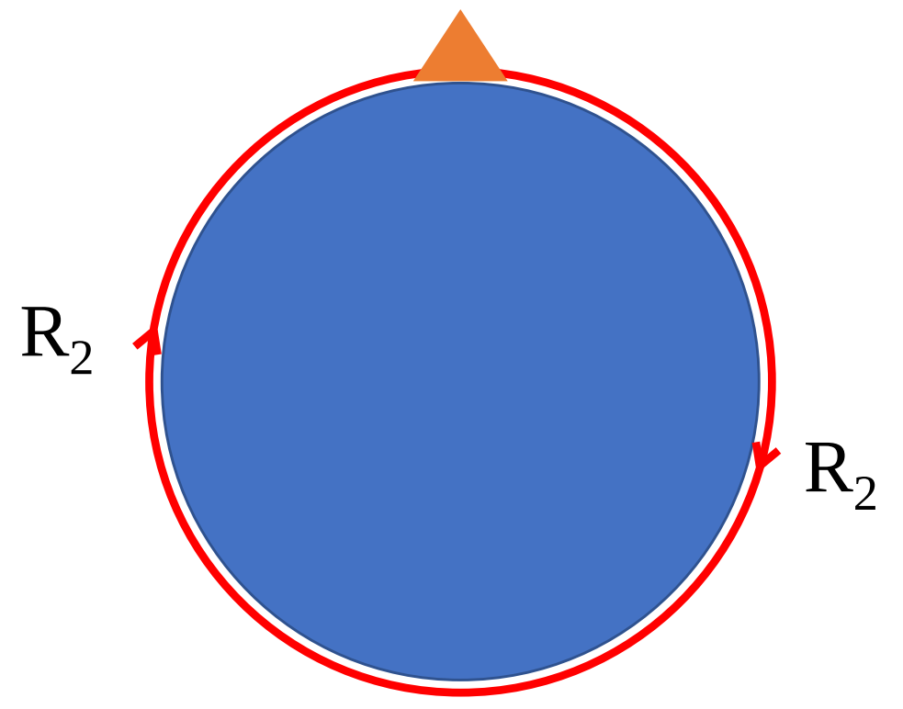

InSight Seismic Data

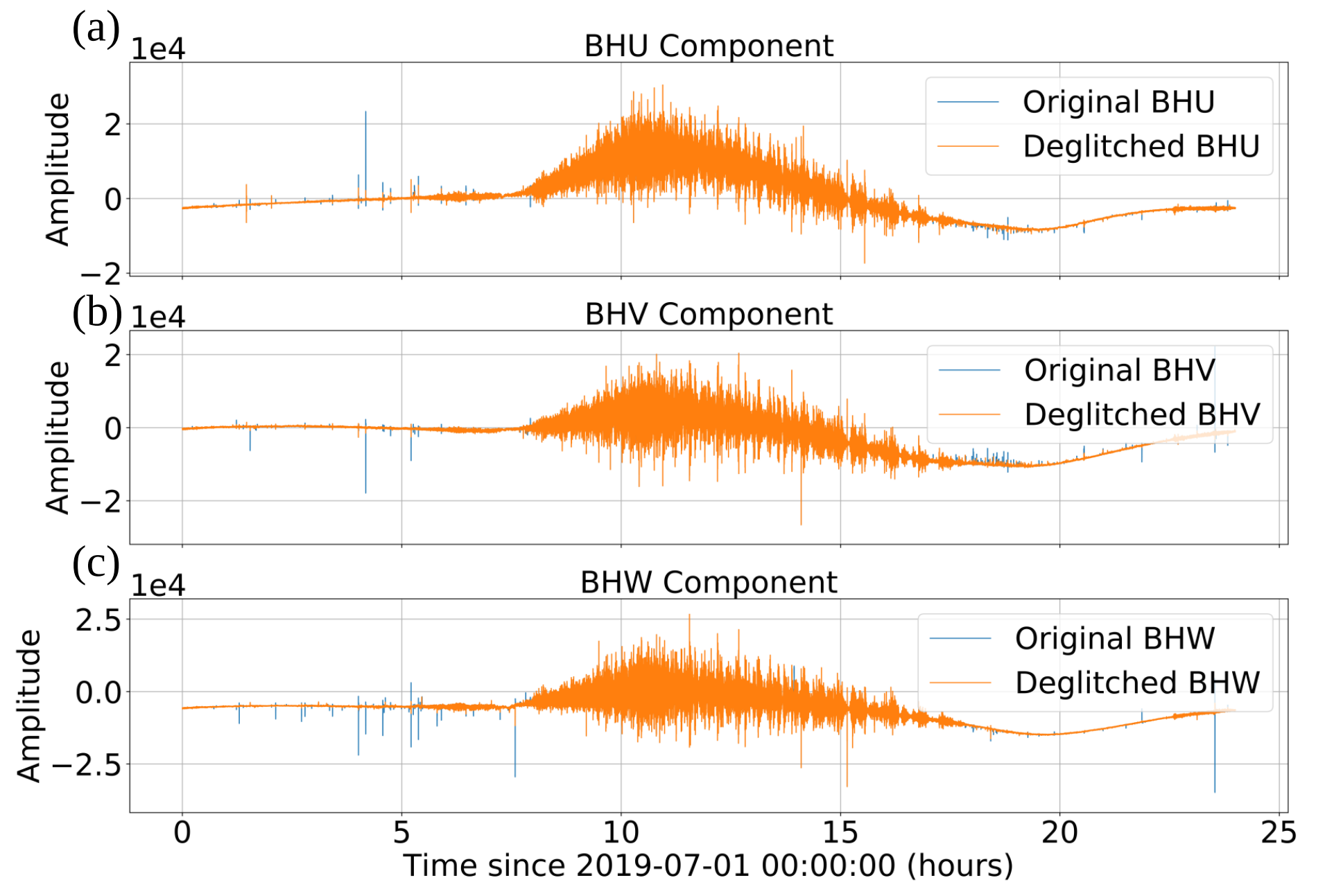

Figure 1. (a) Glitch detection and removal on BHU-component by the Python package SEISglitch (Scholz et al., 2020) on the Martian broadband seismic data recorded on July 1st, 2019. (b) Same as (a) but for BHV-component. (c) Same as (a) but for BHW-component.

Crust-Mantle Boundary (Moho)

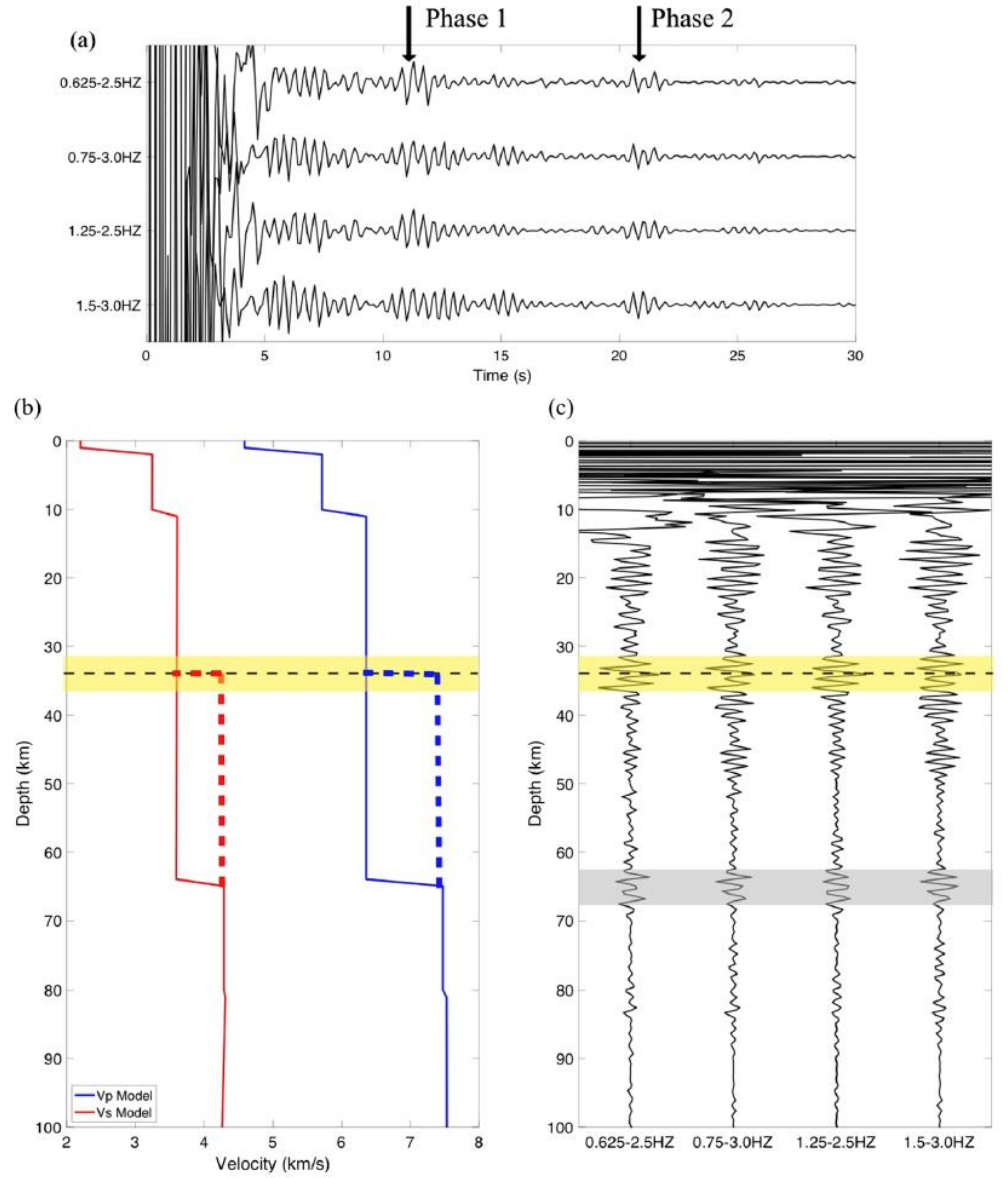

Figure 2. (a) The stacked autocorrelation filtered into different frequency bands. (b) The velocity model (LFAK) (solid line) derived from geophysical-petrological inversion (Khan et al., 2018). The dashed line marks the Moho from our study (c) Depth conversion of the stacked autocorrelation reflectivity series.

Phase 1 at ~11.5s	Phase 2 at ~21s
PmP	SmS
PmP	PmP2
PmP	Upper Mantle Discontinuity
Intracrustal Discontinuity	PmP

Table 1. Possible explanation of Phase 1 at ~11.5s and Phase 2 at ~21s. The interpretation marked in red is the one that we preferred.

Moho Depth	~35km
Vp/Vs ratio	~1.84 (Basalt/Andesite)

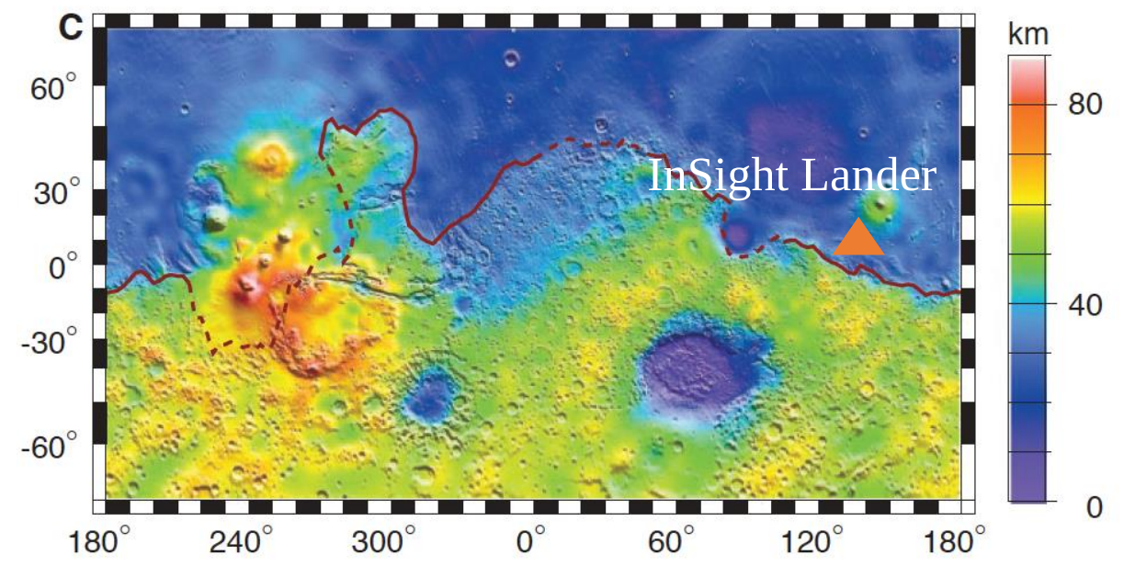

(Zuber et al., 2000)

Basalt: 45 - 52% SiO_2; Andesite: 52 - 63% SiO_2

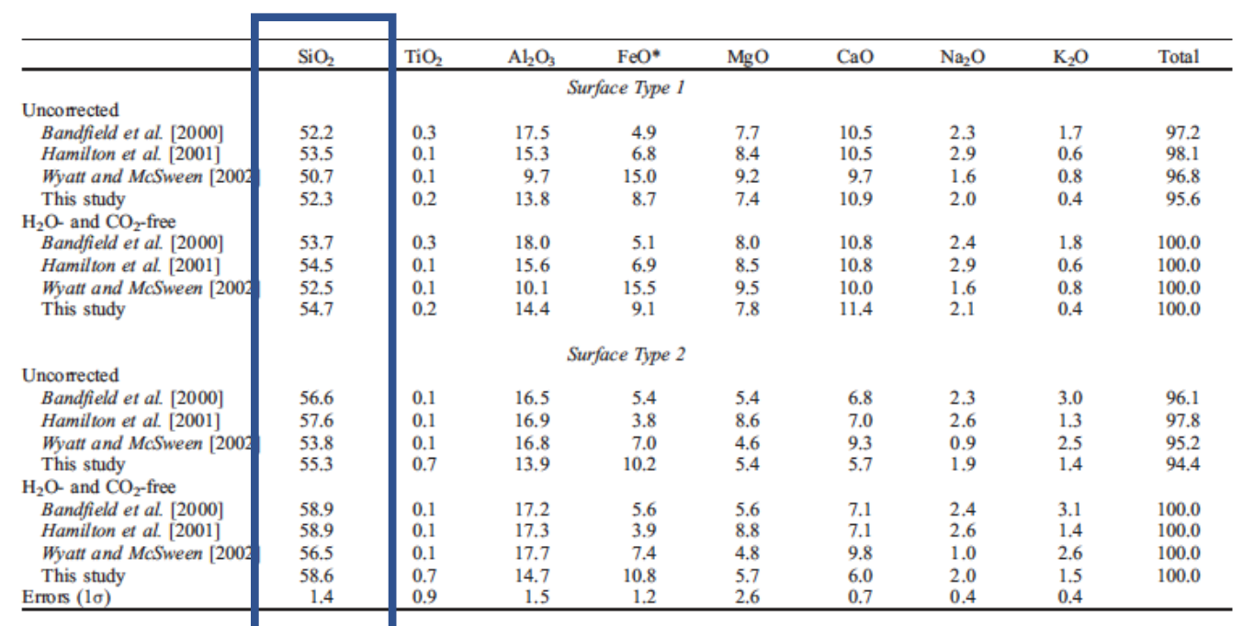

	SiO_2	TiO_2	Al_2O_3	FeO*	MgO	CaO	Na_2O	K_2O	Total
Surface Type 1									
Uncorrected									
Bandfield et al. [2000]	52.2	0.3	17.5	4.9	7.7	10.5	2.3	1.7	97.2
Hamilton et al. [2001]	53.5	0.1	15.3	6.8	8.4	10.5	2.9	0.6	98.1
Wyatt and McSween [2002]	50.7	0.1	9.7	15.0	9.2	9.7	1.6	0.8	96.8
This study	52.3	0.2	13.8	8.7	7.4	10.9	2.0	0.4	95.6
H_2O- and CO_2-free									
Bandfield et al. [2000]	53.7	0.3	18.0	5.1	8.0	10.8	2.4	1.8	100.0
Hamilton et al. [2001]	54.5	0.1	15.6	6.9	8.5	10.8	2.9	0.6	100.0
Wyatt and McSween [2002]	52.5	0.1	10.1	15.5	9.5	10.0	1.6	0.8	100.0
This study	54.7	0.2	14.4	9.1	7.8	11.4	2.1	0.4	100.0
Surface Type 2									
Uncorrected									
Bandfield et al. [2000]	56.6	0.1	16.5	5.4	5.4	6.8	2.3	3.0	96.1
Hamilton et al. [2001]	57.6	0.1	16.9	3.8	8.6	7.0	2.6	1.3	97.8
Wyatt and McSween [2002]	53.8	0.1	16.8	7.0	4.6	9.3	0.9	2.5	95.2
This study	55.3	0.7	13.9	10.2	5.4	5.7	1.9	1.4	94.4
H_2O- and CO_2-free									
Bandfield et al. [2000]	58.9	0.1	17.2	5.6	5.6	7.1	2.4	3.1	100.0
Hamilton et al. [2001]	58.9	0.1	17.3	3.9	8.8	7.1	2.6	1.4	100.0
Wyatt and McSween [2002]	56.5	0.1	17.7	7.4	4.8	9.8	1.0	2.6	100.0
This study	58.6	0.7	14.7	10.8	5.7	6.0	2.0	1.5	100.0
Errors (1σ)	1.4	0.9	1.5	1.2	2.6	0.7	0.4	0.4	

(McSween et al., 2003)

Olivine-Wadsleyite Transition and Core-Mantle Boundary

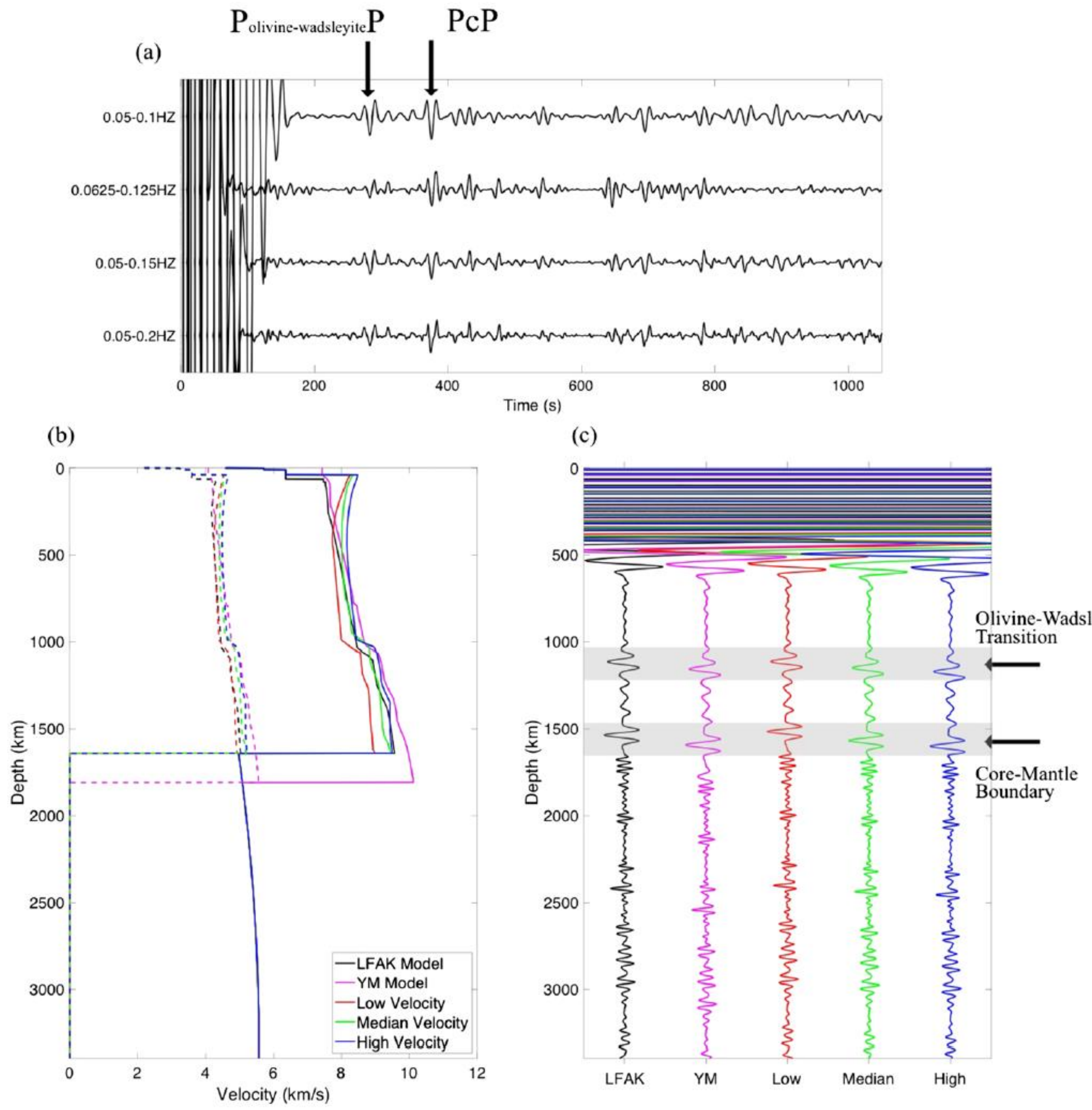

Figure 3. (a) The stacked autocorrelation filtered into different frequency bands. (b) (b) The P (solid line) and S wave (dashed line) velocity model, LFAK model from geophysical-petrological inversion (Khan et al., 2018), YM model from theoretical calculation (Yoshizaki & McDonough, 2020), and three representative velocity models from mineralogical simulation (Panning et al., 2017). (c) Depth conversion of the stacked autocorrelation reflectivity series using different velocity models in (b).

	Autocorrelation Reflectivity	Minerology Simulation (Verhoeven et al., 2005)	Geophysical-Petrological Inversion (Khan et al., 2018)
Olivine-Wadsleyite Transition	$1140 \pm 30\ km$	$\sim 1050-1200\ km$	$\sim 1000-1100\ km$

	Autocorrelation Reflectivity	Geodetic Inversion (Rivoldini et al., 2011)	Solar Tide Detection (Yoder et al., 2003)
Core Radius	$1830 \pm 40\ km$	$\sim 1701-1900\ km$	$\sim 1520-1840\ km$

Table 2. Comparison between the depth of olivine-wadsleyite transition and core radius derived from this study and other measurements.

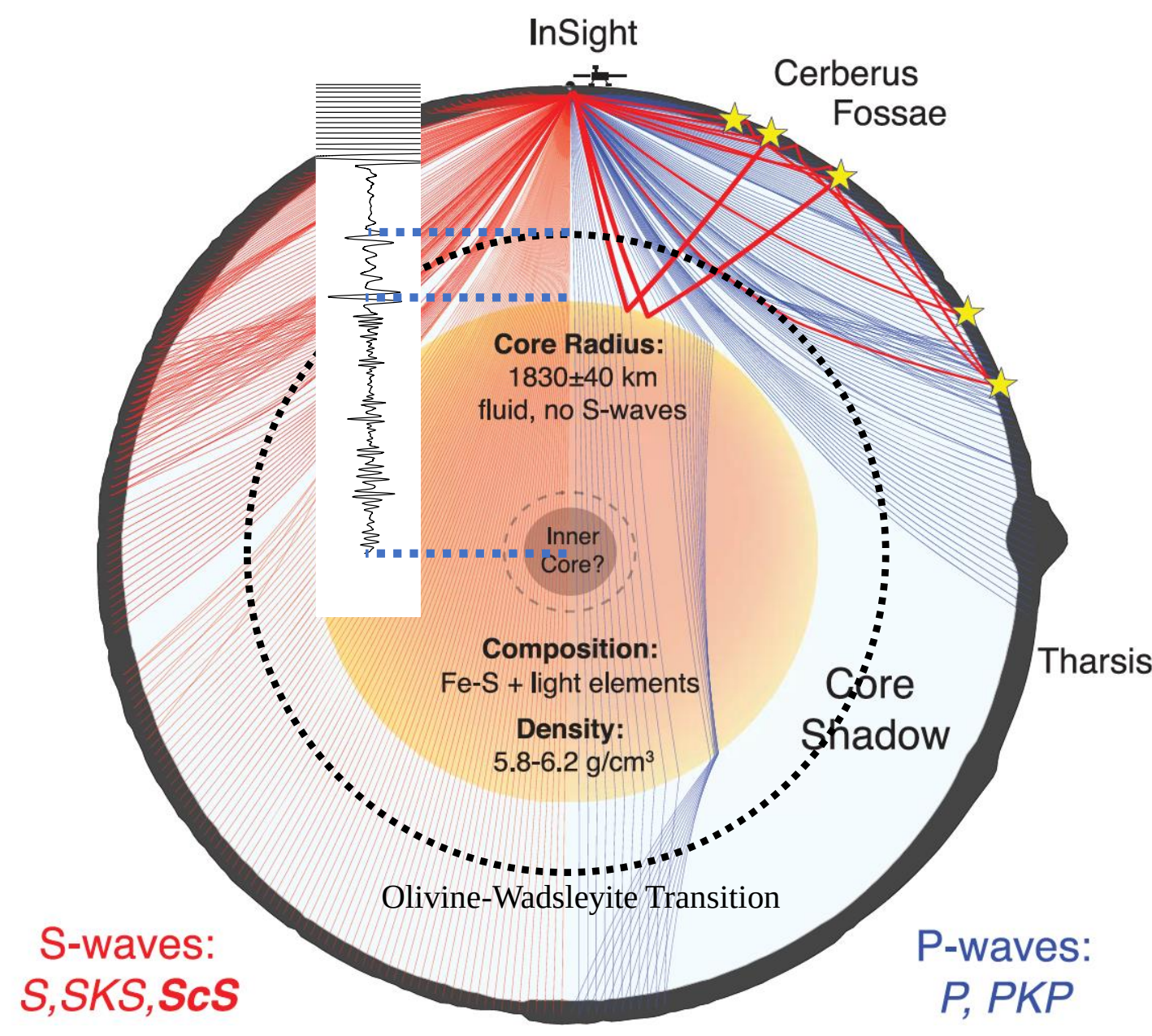

Figure 4. Schema showing Martian Interior (Modified From Figure 3 of Stähler et al. (2021)).

Mars Orbiting Surface Wave (R_2)

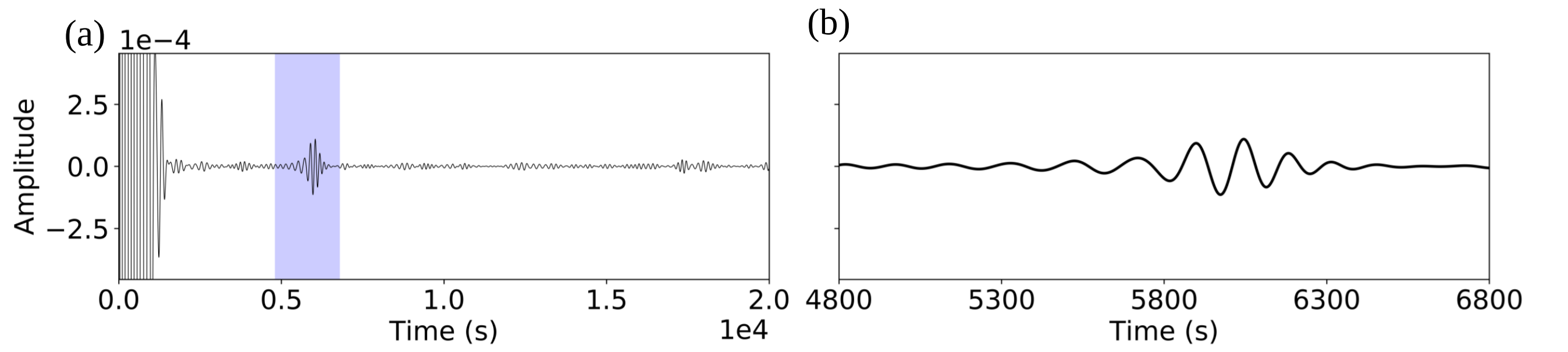

Figure 5. (a) Stacked Autocorrelation filtered between 0.005 and 0.01Hz. The blue area marks the observation of Mars orbiting surface wave. (b) Zoom in the blue area in (a) (4800-6800s).

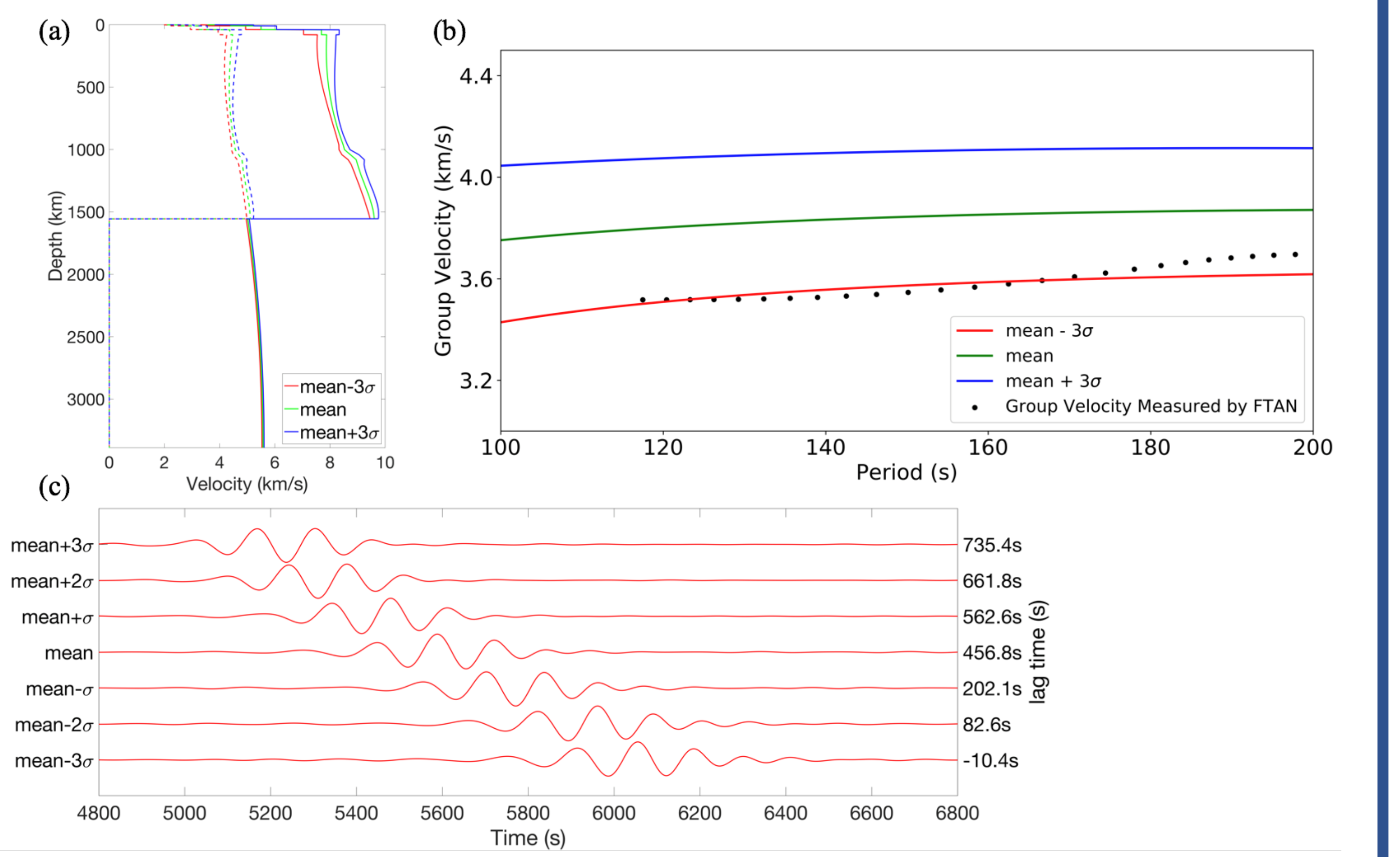

Figure 6. (a) Probabilistic inversion of the Martian velocity models in Stähler et al. (2021). The velocity models range from 3 standard deviations lower to 3 standard deviations higher than the mean velocity. (b) The group dispersion curves for different velocity models shown in (a) (solid lines) and the group velocities measured by frequency time analysis (FTAN) of Figure 5b (black dots). (c) Synthetic seismograms filtered between 0.005 and 0.01Hz for different velocity models shown in (a). The lag time is the cross-correlation time shift between the synthetic seismograms and the stacked vertical-component autocorrelation shown in Figure 5b. The positive lag time means that the observed R_2 phase propagates slower than the synthetics.

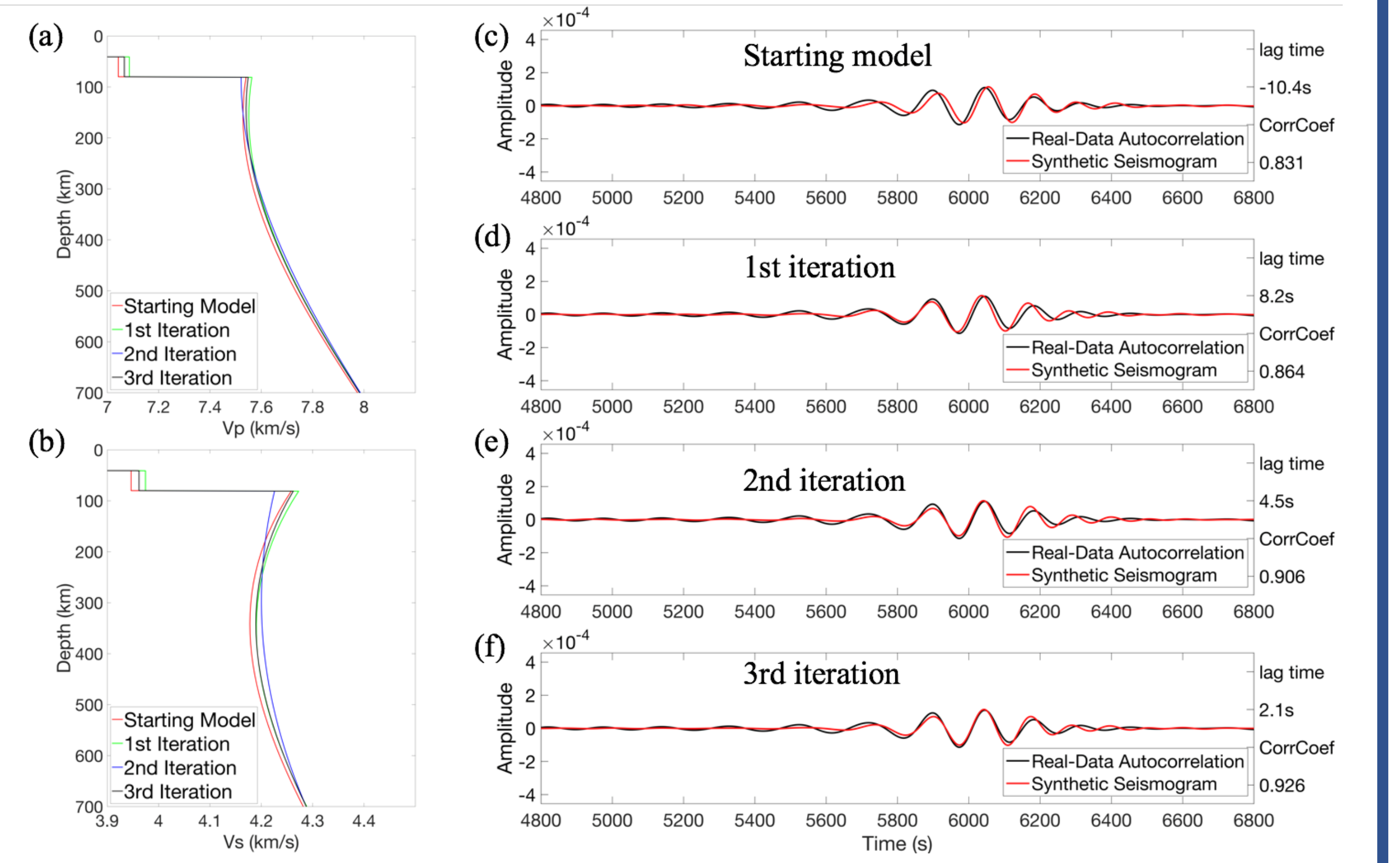

Figure 7. P- and S-wave velocity model of the Martian upper mantle (40-700 km) updated during the Monte Carlo inversion are shown in (a) and (b) respectively. Comparisons between the synthetic R_2 waveforms and real-data autocorrelation (Figure 5b) filtered between 0.005 and 0.01Hz for the starting velocity model (The red model in (a) and (b)) and the velocity models after 1st (The green model in (a) and (b)), 2nd (The blue model in (a) and (b)) and 3rd (The black model in (a) and (b)) iteration are shown in (c) – (f). The correlation time shifts and correlation coefficients between synthetic and observed R_2 waveforms are listed at the right side of (c) – (f). Positive lag time means that the observed R_2 phase propagates slower than synthetics.

Conclusion

1. The crustal thickness beneath the InSight seismic station is 35 ± 2km, consistent with results derived from gravity inversion. The crustal Vp/Vs ratio is about ~1.84, demonstrating that Martian crust is mainly made by basalt or andesite.
2. The olivine-wadsleyite transition (410km on Earth) is observed at 1140 ± 30km depth. The ringwoodite-perovskite transition (660km on Earth) is not observed because the required pressures and temperatures are not reached at the bottom of mantle.
3. The core radius is 1830 ± 40km, consistent with the results derived from geophysical-petrological inversion, geodetic inversion and solar tide detection.
4. Comparing synthetic group dispersion curves (Figure 6b) and seismograms (Figure 6c) from a set of Martian velocity models in Figure 6a, we found that the upper mantle velocity structure is slightly slower than the one derived from the joint inversion of multiple geophysical datasets (Stähler et al., 2021).
5. Monte-Carlo Inversion was employed to provide a velocity model that better fits the Mars orbiting surface waves. The S-wave low-velocity zone extends to ~400km depth, consistent with S-wave shadow zone observation (Khan et al., 2021), geophysical inversion (Khan et al., 2021) and and high-pressure laboratory experiments (Xu et al., 2021).

Reference

Claerbout, J. F. (1968). *Geophysics*.
Deng, S., & Levander, A. (2020). *Geophysical Research Letters*.
Deng, S., & Levander, A. (2022). *Geophysical Research Letters*.
Khan, A., & Connolly, J. A. D. (2008). *Journal of Geophysical Research E: Planets*.
Khan, A., Ceylan, S., van Driel, M., Giardini, D., Lognonné, P., Samuel, H., et al. (2021). *Science*.
McSween, H. Y., Grove, T. L., & Wyatt, M. B. (2003). *Journal of Geophysical Research E: Planets*.
Panning, M. P., Lognonné, P., Bruce Banerdt, W., Garcia, R., Golombek, M., Kedar, S., et al. (2017). *Space Science Reviews*.
Rivoldini, A., Van Hoolst, T., Verhoeven, O., Mocquet, A., & Dehant, V. (2011). *Icarus*.
Schimmel, M., Stutzmann, E., & Ventosa, S. (2018). *Seismological Research Letters*.
Stähler, S. C., Khan, A., Bruce Banerdt, W., Lognonné, P., Giardini, D., Ceylan, S., et al. (2021). *Science*.
Verhoeven, O., Rivoldini, A., Vacher, P., Mocquet, A., Choblet, G., Menvielle, M., et al. (2005). *Journal of Geophysical Research E: Planets*.
Xu, F., Siersch, N. C., Gréaux, S., Rivoldini, A., Kuwahara, H., Kondo, N., et al. (2021). *Geophysical Research Letters*.
Yoder, C. F., Konopliv, A. S., Yuan, D. N., Standish, E. M., & Folkner, W. M. (2003). *Science*.
Yoshizaki, T., & McDonough, W. F. (2020). *Geochimica et Cosmochimica Acta*.
Zuber, M. T., Solomon, S. C., Phillips, R. J., Smith, D. E., Tyler, G. L., Aharonson, O., et al. (2000). *Science*.

Acknowledgement

1. This research was funded by the Department of Earth, Environmental and Planetary Sciences at Rice University
2. The InSight seismic data used in this study was downloaded from the IRIS data center (https://www.iris.edu/hq/sis/insight)